Experimental Investigation of the Three-Dimensional Structure of a Shock Wave/Turbulent Boundary Layer Interaction

R.A. Humble[1] G.E. Elsinga[1] F. Scarano[1] B.W. van Oudheusden[1]

[1]Faculty of Aerospace Engineering
Delft University of Technology, 2629 HS Delft, THE NETHERLANDS

Abstract

Tomographic particle image velocimetry and proper orthogonal decomposition are used to investigate the three-dimensional instantaneous flow organization of an incident shock wave/turbulent boundary layer interaction at Mach 2.1. The results show that the incoming boundary layer contains large-scale coherent motions, in the form of streamwise-elongated regions of low- and high-speed fluid, similar to what has been observed in incompressible turbulent boundary layers. The instantaneous reflected shock foot pattern appears to respond to these regions as they enter the interaction, conforming to the low- and high-speed regions. Its behaviour can be qualitatively decomposed into two types of patterns: an overall streamwise translation and a spanwise rippling. These observations are substantiated by the global eigenmodes of the proper orthogonal decomposition, which contain subspace representations of this phenomenology.

Introduction

Despite sustained scientific interest for over half a century, the interaction between a shock wave and a turbulent boundary layer (SWTBLI) continues to pose significant experimental and theoretical challenges. Such interactions occur ubiquitously in a wide variety of internal and external aerothermodynamic flow problems, and a detailed understanding of the physics remains a necessary prerequisite for accurate flowfield prediction and efficient design of high-speed aerospace vehicles. Reviews of many of the early investigations, concerning two-dimensional (2D) interactions, can be found in [1,14,15]. More recent reviews, with emphasis on the turbulence and unsteadiness properties, including three-dimensional (3D) interactions, can be found in [5,6,27].

SWTBLIs are often characterized as compression ramp or incident shock wave interactions. Common features of both typically include an incoming boundary layer subjected to an adverse pressure gradient. For sufficiently strong interactions, involving boundary layer separation, the mean pressure distribution shows a plateau in the separated flow region. A significant amplification of the turbulence levels occurs across the interacting shock wave system. This system undergoes a complicated motion at dominant frequencies typically much lower than the characteristic frequency U_∞/δ [6]. Farther downstream, the boundary layer undergoes a relaxation process that persists for several boundary layer thicknesses.

With the development of laser and digital imaging technology, nonintrusive flow diagnostic techniques, such as particle image velocimetry (PIV) in particular, have led to an escalation in the creative interpretations of SWTBLI phenomenology. Relatively recent work in compression ramp interactions suggests that the incoming boundary layer plays an important role in the large-scale unsteadiness. Results obtained by Ünalmis & Dolling [29] and Beresh *et al.* [3] indicate that at least some of the unsteadiness is driven by turbulent fluctuations within the upstream boundary layer. Using PIV in the streamwise–spanwise plane, Ganapathisubramani *et al.* [11] have shown that there is a relationship between large-scale coherent motions within the incoming boundary layer and the separation region. The instantaneous separation line was found to be undulated in a manner that conforms to these regions, and the authors concluded that the regions could contribute to the large-scale unsteadiness of the separation region. It is not yet clear, however, whether or not the same mechanisms are present in the case of a shock reflection [23].

While the studies mentioned above have given insight into the phenomenology involved, the inability to make direct instantaneous volumetric measurements necessitates various assumptions to be made to link these reduced-dimensional representations to the 3D structure of the flow organization. In this respect, an instantaneous volumetric characterization of the flowfield is more appropriate for revealing the complex spatial interrelationships involved. Computational fluid dynamics (CFD), making use of large eddy simulation (LES) and direct numerical simulation (DNS), have therefore played an instrumental role in explicating the characteristic 3D dynamical features of wall-bounded turbulence (e.g., [32,20]), as well as those observed in SWTBLIs (e.g., [23,31]). Yet the attendant Reynolds number limitation leaves the phenomenology at high Reynolds numbers very much an open question.

There has thus been a strong motivation within the experimental community to be able to capture 3D flow features instantaneously. PIV in particular, has been used extensively in the measurement of turbulent flows, due to its ability to capture the instantaneous velocity field in a plane. Recently, the technique has been extended to the measurement of particle motion within a 3D measurement volume, with the introduction of tomographic PIV [9]. This technique provides instantaneous volumetric 3D velocity information using the principles of optical tomography. While the initial applications of tomographic PIV have been in low-speed, low-Reynolds number boundary layer flows (e.g., [25]), its extension to the supersonic flow regime has been recently achieved [7]. Its application to the SWTBLI problem is therefore considered to be well-posed.

With the increasingly large amount of data that can be obtained, attention has also been focused on strategies that lead to a reduction of the data while ensuring that the dominant features are maintained. This can be achieved by statistical techniques, such as the proper orthogonal decomposition (POD) in particular. This technique has been introduced into fluid mechanics (see [4]) as a tool to highlight coherent motions within turbulent flows, as well as to facilitate the development of a low-order description of the overall dynamics. It has been applied to a variety of flow problems of relevant interest, including boundary layers [2] and compressible flows [21], as well as the SWTBLI problem [19]. PIV data is particularly suited for POD analyses since the entire velocity field is available, leading to the construction of global eigenmodes. Yet this complementary approach has so far not been reported using 3D experimental data of SWTBLIs.

The present paper aims to investigate the 3D instantaneous flow organization of an incident SWTBLI using tomographic PIV, and then to statistically decompose the flowfield into a series of modes that capture the most dominant components using the POD. A brief outline of the working principles of tomographic PIV and a mathematical outline of the POD now follows. A description of the flow facility, experimental apparatus, and data acquisition and processing is then provided. Results, consisting of both 2D and 3D instantaneous velocity measurements of the interaction are then presented, followed by the global eigenmodes obtained from the POD analysis. Finally, summary and conclusions are given.

Techniques and Experimental Procedure
Working Principles of Tomographic PIV

Tomographic PIV is based on the principles of optical tomography, which essentially reconstructs a 3D volume (the object) on the basis of a set of simultaneous images taken from several different viewing directions. A detailed discussion of the technique and its principles is given by Elsinga *et al.* [9]. Briefly, tracer particles are illuminated within a measurement volume by a pulsed light source. The 3D light distribution constitutes the object. The scattered light is captured simultaneously from several different viewing directions by CCD cameras. The object is then reconstructed as a 3D light intensity distribution using the multiplicative algebraic reconstruction technique (MART) [16]. In this approach, the object is represented in discretized form as a 3D array of cubic voxel elements, and the set of linear equations, which model the imaging system, are solved iteratively. The object is given by a series of 3D voxels in physical space (X, Y, Z), with the light intensity given by $E(X, Y, Z)$. The projection of the light intensity distribution E onto each image pixel (x_i, y_i) gives the image intensity distribution $I(x_i, y_i)$. The system of equations relating E and I is given by

$$\sum_{j \in N_i} w_{i,j} E\left(X_j, Y_j, Z_j\right) = I\left(x_i, y_i\right) \qquad (1)$$

where $w_{i,j}$ is the weighting coefficient that describes the contribution of the jth voxel intensity $E(X_j, Y_j, Z_j)$ to the ith pixel intensity $I(x_i, y_i)$. N_i is the total number of voxels in the line-of-sight corresponding to the ith pixel (x_i, y_i). In practice, the MART is implemented as an iterative technique, with the update of the system of equations based on the ratio between the measured pixel intensity and the projection of the object, along with an appropriate scalar relaxation parameter. The iterative object update reads as

$$\sum_{j \in N_i} w_{i,j} E\left(X_j, Y_j, Z_j\right)^{k+1}$$
$$= \left(I\left(x_i, y_i\right) \bigg/ \sum_{j \in N_i} w_{i,j} E\left(X_j, Y_j, Z_j\right)^{k}\right)^{\mu w_{i,j}} \qquad (2)$$

where μ is the scalar relaxation parameter, with the property that $\mu \in [0,1]$. Since accurate reconstruction relies on accurate triangulation of the camera views, the difference between the image coordinates and those within the reconstructed volume is established through a calibration procedure, similar to the one followed in stereoscopic PIV, where a calibration target is recorded by each camera at several depth positions within the volume. This provides the viewing directions and fields-of-view from each camera. After the acquisition of recorded images from the experiment, a self-calibration procedure is then carried out, which allows the above-mentioned triangulation to be corrected up to a residual disparity below 0.2 pixels [30]. The 3D mapping function is corrected accordingly. The velocity fields are finally determined by a 3D cross-correlation of the reconstructed particle distributions.

Proper Orthogonal Decomposition

The POD is a statistical technique that decomposes a signal into a basis of nonspecified functions that contain the maximum energy of the signal in the fewest modes (see [17]). In the present study, a decomposition of the time variation of the flowfield is made. Consider a system where N data measurements are simultaneously taken at M time instants t_n, such that the samples are uncorrelated and linearly independent. The data represent velocity obtained from the PIV study. The mean velocity at a point $\overline{u}(\mathbf{x})$ is subtracted from the instantaneous velocity $u(\mathbf{x}, t_n)$, leaving fluctuations from the mean $u'(\mathbf{x}, t_n)$, where $\mathbf{x} \in [x, y, z]$. The POD extracts k time-independent orthonormal basis functions, empirical eigenfunctions, or eigenmodes, $\psi_k(\mathbf{x})$, and time-dependent orthonormal amplitude coefficients, $a_k(t_n)$, such that the reconstruction

$$u'\left(\mathbf{x}, t_n\right) = \sum_{k=1}^{M} a_k\left(t_n\right) \psi_k\left(\mathbf{x}\right) \qquad (3)$$

is optimal, in the sense that the functions ψ maximize the normalized averaged projection of ψ onto u', viz.

$$\max_{\psi} \frac{\left\langle \left|\left(u', \psi\right)\right|^2\right\rangle}{\left\|\psi\right\|^2} \qquad (4)$$

Here, $\left\| \cdot \right\|$ denotes the L^2-norm $\left\|f\right\|^2 = (\cdot, \cdot)$, where $(\cdot, \cdot)$ is the standard Euclidean inner product. $\left| \cdot \right|$ is the modulus. The ergodic hypothesis is invoked so that ensemble averages $\langle \cdot \rangle$ represent time averages. The problem can be recast as the solution to the following Euler–Lagrange integral equation

$$\int_{\Omega} \left\langle u'\left(\mathbf{x}\right) \otimes u'^*\left(\mathbf{x}'\right)\right\rangle \psi\left(\mathbf{x}'\right) \mathrm{d}\mathbf{x}' = \lambda \psi\left(\mathbf{x}\right) \qquad (5)$$

where Ω is the flow domain, $\otimes$ is the tensor product and $*$ denotes complex conjugation. The kernel of Eq. (5) is the averaged autocorrelation tensor, which for a series of snapshots containing data at a finite number of discrete points is given by

$$R\left(\mathbf{x}; \mathbf{x}'\right) = \frac{1}{M} \sum_{n=1}^{M} u'\left(\mathbf{x}, t_n\right) u'\left(\mathbf{x}', t_n\right) \qquad (6)$$

The non-negative and self-adjoint properties of $R(\mathbf{x};\mathbf{x}')$ ensure that all eigenvalues are real and non-negative, and can therefore be ordered $\lambda_k \geq \lambda_{k+1} \geq \ldots \geq 0$. As first proposed by Sirovich [26], the *method of snapshots* is implemented in the present study to make use of the fact that $u'(\mathbf{x}, t_n)$ and $\psi_k(\mathbf{x})$ span the same linear space. This enables the POD eigenmodes to be written as a linear sum of the data vectors

$$\psi_k\left(\mathbf{x}\right) = \sum_{n=1}^{M} \Phi_n^k u'\left(\mathbf{x}, t_n\right), \qquad k = 1, \ldots, M \qquad (7)$$

where Φ_n^k is the nth component of the kth eigenvector. The eigenmodes can then found by solving the following eigenvalue problem

$$C\Phi = \lambda\Phi \qquad (8)$$

The eigenvectors of the $N \times N$ matrix R are therefore found by computing the $M \times M$ matrix C—an attractive method since in the present study $M \ll N$ [where $M \sim 100$ and each snapshot contains vector fields of size $N = 144(N_x) \times 74(N_y) \times 19(N_z) \approx 200\,000$]. The reconstruction of an original snapshot using an arbitrary number of modes K can be performed with

$$u\left(\mathbf{x},t_n\right)=\overline{u}\left(\mathbf{x}\right)+\sum_{k=1}^{K}a_k\left(t_n\right)\psi_k\left(\mathbf{x}\right) \quad\quad (9)$$

The total energy of the flow is defined as the mean square fluctuating value of velocity, and is given by the sum of the eigenvalues λ_k. Each eigenmode can therefore be assigned an energy percentage E_k based on the eigenmode's eigenvalue, such that

$$E_k=\lambda_k\Big/\sum_{n=1}^{M}\lambda_n \quad\quad (10)$$

Experimental Setup

Experiments were performed in the blow-down transonic-supersonic wind tunnel (TST-27) of the High-Speed Aerodynamics Laboratories at Delft University of Technology. The facility generates flows in the Mach number range 0.5–4.2 in a test section with maximum dimensions of 270mm×280mm. The Mach number is set by means of a continuous variation of the throat section and flexible nozzle walls. The tunnel operates at unit Reynolds numbers ranging from 30×10^6 to 130×10^6m^{-1}, enabling an operating use of approximately 300s. In the present study, the tunnel was operated at a nominal Mach number of 2.1 (U_∞=503m/s) with a stagnation pressure of 282kPa and stagnation temperature of 273K.

The boundary layer developing along the side-wall was chosen in order to match the flow scales with the resolution capabilities of the measurement technique. The boundary layer developed along a smooth surface for approximately 2m under nearly adiabatic flow conditions. On entering the test section, the boundary layer thickness was approximately δ_{99}=20mm with Re_θ=4.92×10^4. The experimental conditions are summarized in table 1. Mean and turbulence statistics of the undisturbed boundary layer and a similar interaction have been reported by Humble et al. [18].

Parameter	Quantity
M_∞	2.07
U_∞, m/s	503
δ_{99}, mm	20
P_0, kPa	282
T_0, K	273
Re_θ	4.92×10^4

Table 1. Summary of experimental conditions.

A 70mm long shock generator imposing a deflection angle of 10° was placed in the freestream flow to generate the incident shock wave. The generator was mounted vertically in the centre of the test section on an 80cm long sting and spanned approximately 65% of the test section height. A schematic representation of the experimental arrangement is shown in figure 1. The origin of the reference coordinate system is located at the extrapolated wall impingement point of the incident shock wave, with x measured in the streamwise (or longitudinal) flow direction, y in the spanwise (or transverse) direction measured from the centre of the test section, and z in the vertical (or wall-normal) direction. The corresponding velocity components are denoted by u, v, w, respectively. Note that the shock generator is sufficiently long to prevent the expansion fan at its shoulder from influencing the measurement domain.
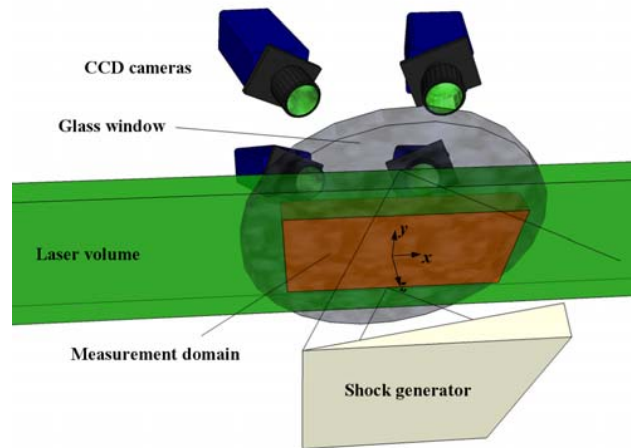

Figure 1. Schematic of experimental arrangement. Note that the shock generator's sting has been omitted for clarity.

To highlight some basic qualitative features of the interaction, figure 2 shows a spark Schlieren visualization. The impingement and passage of the incident shock wave through the boundary layer can be observed, as well as compression waves, which begin to form upstream within the incoming boundary layer as the reflected shock foot, which coalesces to form the reflected shock wave. Its large-scale, three-dimensional motion is evident. Farther downstream, the boundary layer undergoes a recovery process.
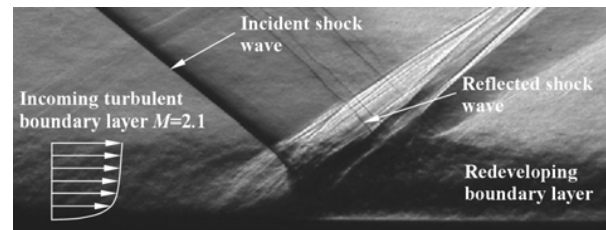

Figure 2. Spark Schlieren of the interaction.

PIV System

Flow seeding and illumination constitute critical aspects of PIV in high-speed flows. A 10mm diameter probe was inserted into the settling chamber to seed the upstream boundary layer. Titanium dioxide (TiO$_2$) particles with a nominal diameter of 170nm and a bulk density of 200kg/m^3 were adopted as tracers. The particle relaxation time across the incident shock wave (based on particles with a nominal diameter of 50nm) has been determined to be $\tau_p\sim$2μs, corresponding to a frequency response $f_p\sim$500kHz [18].

The seeded flow was illuminated by a Spectra-Physics Quanta Ray double-pulsed Nd:Yag laser, with 400mJ pulsed energy and a 6ns pulse duration at wavelength 532nm. A probe inserted into the flow downstream of the test section provided laser light access, and shaped the light beam into a volume using light optics (see table 2). Before light entered the probe, a knife-edge slit filter was used to remove the low-energy fringes present, and to give a better approximation of a top-hat light intensity distribution. To minimize reflections, illumination was almost tangent to the wall. The laser pulse separation was 2μs, allowing a particle displacement in the freestream of approximately 1mm ($\approx$20 voxels).

Data Acquisition and Processing

A dataset of order 100 particle image quadruplets were recorded by four LaVision Imager Pro X 4M CCD cameras with a 2048×2048 pixel-sized sensor. Only 1216 pixels were used in the spanwise direction given the aspect ratio of the investigated flow region. At the same time, this enabled an increased recording rate of 10Hz. The digital imaging resolution was 23pixels/mm. The solid angle enclosed between all four cameras was 40°×35° in the streamwise–wall-normal, and spanwise–wall-normal planes, respectively. Each camera was equipped with a Nikon 60mm focal objective, with Scheimpflug adapters to maintain focus of the measurement domain. The cameras were fitted with a narrow-band-pass 532nm filter to minimize ambient light interference. The two cameras in forward-scatter had f-number $f_\#=8$ and the two cameras in back-scatter had f-number $f_\#=11$. The tomographic PIV recording parameters are summarized in table 2.

Parameter	
Field-of-view	$75(L)\times40(W)\times10(H)mm^3$
Interrogation volume	$2.1\times2.1\times2.1mm^3$
Digital imaging res.	23pixels/mm
Objective focal length	$f=60mm$
f-number	$f_{\#1}=8, f_{\#2}=11, f_{\#3}=8, f_{\#4}=11$
Pulse delay	$2\mu s$

Table 2. Summary of tomographic recording parameters.

Synchronization between the cameras, laser, and image acquisition was accomplished by a LaVision programmable timing unit controlled through DaVis 7.3 software, which was also used in the data recording, volume calibration, self-calibration, as well as the 3D cross-correlation based interrogation that yielded the velocity vector fields. Reconstructed volumes were discretized at 20voxels/mm³. The particle images were interrogated using a final window size of 42×42×42 voxels with an overlap factor of 75%.

Particle images were preprocessed before reconstruction. This involved subtracting the time-minimum background intensity, as well as a sliding spatial minimum. Gaussian smoothing using a 3×3 kernel was then applied to reduce image noise. Postprocessing involved identifying erroneous vectors using the universal median test with a maximum median deviation set at 2.5. To ease visualization, the instantaneous velocity fields were filtered using a 3D Gaussian filter based on a kernel of 3×3×3 points. The expected measurement uncertainty was inferred from previous experiments by comparing tomographic and stereoscopic PIV and yielded uncertainty levels of 2–3%. Although no direct validation of the tomographic PIV technique is given here, a comparison with stereoscopic PIV and hot-wire anemometry in an incompressible turbulent boundary layer has been made [8].

Results and Discussion
2D Instantaneous Flow Organization

To first shed some light on the flow features of the interaction, 2D instantaneous velocity distributions are shown in figure 3 at $z/\delta=0.12$. The results are extracted from the tomographic results and are chosen to exemplify the typical flow features observed. Velocity vectors are shown in a convective frame of reference of $0.8U_\infty$. The results capture the incoming boundary, as well as the compression region, which contains the reflected shock foot that initiates at approximately $x/\delta=-1.5$. Boundary layer recovery is observed farther downstream. Figure 3(a) shows the streamwise velocity distribution, and reveals distinct, large-scale regions within the incoming boundary layer of relatively low- and high-speed fluid. These regions are parallel to the wall and elongated

in the streamwise direction. Large velocity differences of up to 100m/s ($0.2U_\infty$) can be observed between these low- and high-speed regions. Because of the limited size of the measurement domain and number of measurement volumes, it is not possible to accurately determine their characteristic geometry (in particular, their streamwise length). However, they appear to have a streamwise length of at least 2δ based on the extent of the measurement domain.

The corresponding spanwise velocity distribution is shown in figure 3(b). Note that the spanwise velocity range is significantly smaller than the other components. The spanwise component appears to be less coherent along both the streamwise and spanwise directions compared with the streamwise component. Patches of spanwise velocity typically form spatially compact regions, which persist throughout the interaction. The corresponding wall-normal velocity distribution is shown in figure 3(c). Relatively small fluctuations are present within the incoming boundary layer. Large positive fluctuations of the order of 100m/s ($0.2U_\infty$) can be observed within the compression region, corresponding to the lifting of the flow. Farther downstream, the redeveloping boundary layer becomes populated with spatially compact regions of negative wall-normal velocity, consistent with the formation of a mixing-type layer [23].
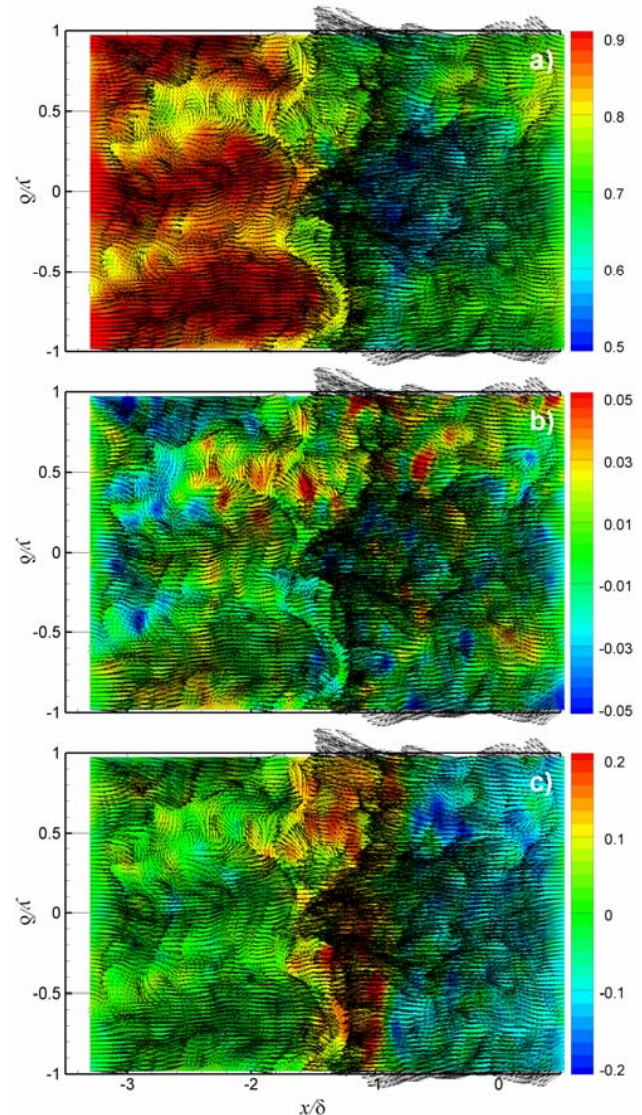

Figure 3. Instantaneous velocity distributions at $z/\delta=0.12$: (a) u/U_∞; (b) v/U_∞; (c) w/U_∞. Velocity vectors are shown in a convective frame of reference of $0.8U_\infty$. Results have been extracted from the tomographic results.

3D Instantaneous Flow Organization

The tomographic results are more appropriate for revealing the 3D instantaneous structure of the interaction. Figure 4 shows a series of uncorrelated measurement volumes containing instantaneous streamwise velocity. The measurement domain extends the range $z=0.1$–0.6δ. [Note that figure 4(a) corresponds to figure 3(a).] For the purposes of illustration, three values of streamwise velocity isosurface are displayed in each volume; namely, isosurfaces of relatively high-speed ($0.9U_\infty$) are shown in red, isosurfaces of intermediate velocity ($0.75U_\infty$) are shown in green, and isosurfaces of relatively low-speed ($0.55U_\infty$) are shown in blue. Velocity vectors in the streamwise–wall-normal plane are shown coloured with streamwise velocity. The results illustrate some additional features not readily apparent in the preceding cross-sectional results. Figure 4(a) shows that the widths of the low- and high-speed streamwise-elongated regions can vary appreciably in the wall-normal direction. Figure 4(b) shows that the high-speed regions can appear interconnected, although this is more likely to be due to the finite streamwise extent of a low-speed region.

The streamwise-elongated regions appear to have a limited spanwise extent. The spanwise dimensions of the low-speed regions are typically within the range $\Delta y=4$–10mm (or 0.2–0.5δ), as confirmed by the statistical analysis performed by Elsinga *et al.* [7] within the undisturbed boundary layer of the present study. This is consistent with the range of 0.25–0.5δ reported by Ganapathisubramani *et al.* [12] within a Mach 2 boundary layer at $z=0.16\delta$, as well as with incompressible turbulent boundary layer research, such as the study performed by Tomkins and Adrian [28] at $Re_\theta=7705$, who report low-speed regions within a spanwise range of 0.15–0.3δ at $z=0.2\delta$. These regions have been found to contribute significantly to the kinematic Reynolds shear stress [13].

On the other hand, such periodic regions in the present data are not ubiquitous. For instance, figure 4(b) shows that the streamwise alignment of the streamwise-elongated regions is not perfect, and there is evidence of appreciable waviness. Figure 4(c) shows that these regions can sometimes span almost the complete measurement domain, where it appears that no obvious spanwise periodicity can be inferred. It is important to remark, however, that the spatial organization of all these regions disappears after data averaging, indicating that they are not stationary.

One of the new aspects of this study is that the structure of the reflected shock foot, inferred from the velocity isosurfaces within the compression region ($x/\delta\approx-1.5$), exhibits various types of behaviour. Although it cannot be stated with certainty that these isosurfaces are indicative of the reflected shock foot's position, inspection of the velocity vectors suggests that a qualitative relationship exists [e.g., see figure 3]. Discussion of these isosurfaces will therefore pertain to the reflected shock foot itself. With this caveat in mind, figure 4 shows some interesting features. Figures 4(a, b) show the reflected shock foot undergoes spanwise undulations of the order of 0.5δ. In contrast, figure 4(c) shows a relatively uniform reflected shock foot displaced in the streamwise direction. Other measurement volumes typically show the same fundamental features, and we therefore qualitatively decompose the reflected shock foot behaviour into two types of patterns: an overall streamwise translation and a spanwise rippling.

Closer inspection reveals that these patterns are associated with the instantaneous flow organization of the incoming boundary layer. Figure 4 (as well as numerous other measurement volumes), exemplifies the behaviour that when the reflected shock foot is encountered by a relatively high-speed region, it appears relatively downstream. Conversely, when it is encountered by a relatively low-speed region, it appears relatively upstream. The reflected shock foot therefore appears to conform to the low- and high-speed streamwise-elongated regions within the incoming boundary layer. This is consistent with the observations reported by Ganapathisubramani *et al.* [11], on the basis of wall-parallel planar measurements in a compression ramp flow. A cursory proposal therefore, is that the streamwise translation pattern is associated with the mean level of incoming momentum, whereas the spanwise rippling pattern is due to its spanwise variation.
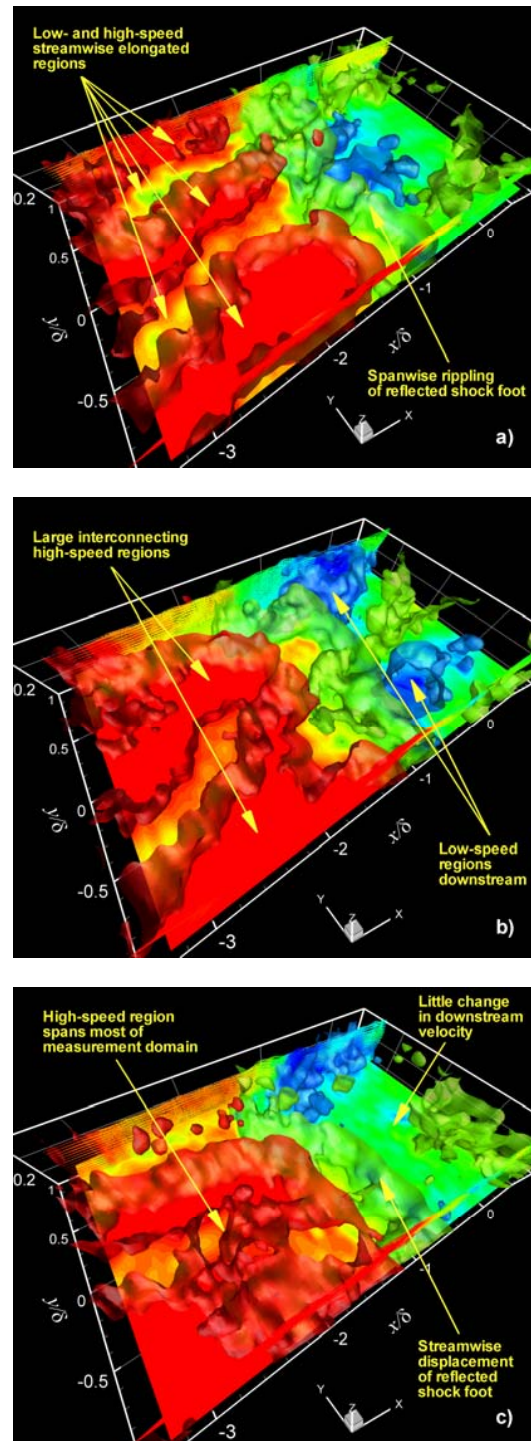

Figure 4. Instantaneous flow organization of the interaction. Isosurfaces of streamwise velocity are shown; relatively high-speed ($0.9U_\infty$) in red, intermediate ($0.75U_\infty$) in green, and relatively low-speed ($0.55U_\infty$) in blue. Velocity vectors are shown flooded with streamwise velocity.

Global POD Eigenmodes

Having made some important observations regarding the phenomenology of the incoming boundary layer and its association with the flow organization of the interaction, we now wish to statistically decompose the flowfield into a series of modes that represent the most dominant components. A statistical evaluation of the velocity fluctuations is therefore carried out using the POD. The decomposition returns global eigenmodes, which can each be considered as capturing an independent predominant characteristic of the flow, and can be viewed as a perturbation of the mean flow. As the motivating prelude, figure 5 shows the modal energy and cumulative modal energy distributions.
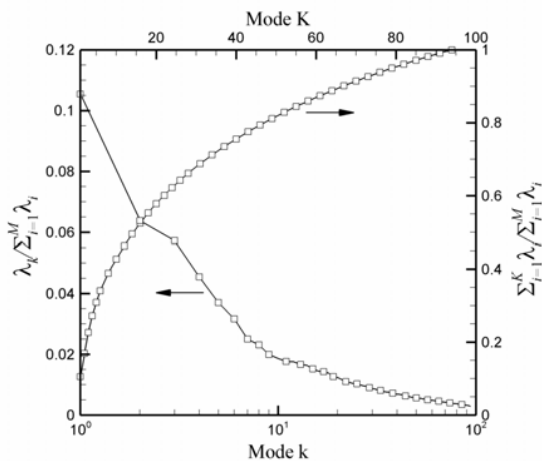

Figure 5. Modal energy content for the kth eigenmode and cumulative modal energy content for the Kth cumulative sum.

The modal energy distribution reveals that the first eigenmode is the most dominant, and that only a limited number (say < 10) contain an appreciable fraction of the total energy. We therefore restrict our attention to discussing these eigenmodes. The cumulative modal energy distribution shows that over 60 modes are required to capture 85% of the total energy; a relatively poor energy convergence compared with other POD analyses of boundary layers (e.g., [2]), where a larger amount of energy is captured by relatively fewer eigenmodes (the first three modes essentially capture the entire flowfield in ref. [2]). This discrepancy is attributed to the comparatively high Reynolds number of the present study, as well as the presence of random noise and occasional poor data quality naturally present in experimental data, which contribute to flattening the eigenspectra by transferring energy towards the higher-order eigenmodes. The present eigenmodes are still considered capable of providing a basis for discussion, however, since conclusions will be drawn that are consistent with the observations made in the instantaneous realizations.

The streamwise and vertical components of the first eigenmode are shown in figures 6(a, b), respectively, with the modal number and energy content shown inset. One caveat before proceeding: Data for $y/\delta > 0.5$ contaminated the eigenmode constructions due to unreliable velocity measurements related to the poor distribution of laser light in this region. Thus, only data for $y/\delta < 0.5$ are used in the analysis. Furthermore, as the temporal coefficients associated with each eigenmode for a particular realization can be either positive or negative, only the relative changes of sign within an eigenmode are important. Figure 6(a) portrays relatively large streamwise fluctuations within the incoming boundary layer that are energetically associated with a broad spanwise region of fluctuations within the reflected shock foot. The superposition of these fluctuations onto the mean flow

returns a streamwise displacement of the reflected shock wave; a behaviour that can be observed in the instantaneous realizations [e.g., figure 4(c)]. Thus, it appears that this eigenmode captures the streamwise translation component of the observed reflected shock foot patterns. The corresponding vertical component depicted in figure 6(b) contains two broad regions of opposed vertical velocity fluctuations within the reflected shock foot and incident shock regions, respectively. The superposition of these fluctuations onto the mean flow returns a contraction/expansion of the interaction. Therefore, the simple model described by the first eigenmode is that positive streamwise fluctuations within the incoming boundary layer correspond to a downstream displacement of the reflected shock foot, accompanied by a decrease in the size of the interaction, and vice versa.

The streamwise and vertical components of the second eigenmode are shown in figures 6(c, d), respectively, and portray a rather different organization. Figure 6(c) shows two large-scale regions of relatively uniform opposed streamwise velocity fluctuations, oriented parallel to the wall and elongated in the streamwise direction. The width of these regions is approximately δ, and they extend the streamwise length of the measurement domain. Note the amplification in fluctuation magnitude throughout the interaction. Such an organization can be viewed as a subspace bifurcation, where the term *bifurcation* refers to the qualitative changes observed. Bifurcations lead to an increase in the number of spatially extended subspace regions with definite sign. Figure 6(c) therefore shows a region that bifurcates into two large-scale regions of opposite sign. These features can be thought of as subspace representations of the low- and high-speed streamwise-elongated regions observed within the incoming boundary layer. The superposition of these fluctuations onto the mean flow returns an undulating pattern of the reflected shock foot; a behaviour that can be observed in the instantaneous realizations [e.g., figures 4(a, b)]. Thus, it appears that this eigenmode captures the spanwise rippling component of the observed reflected shock foot patterns. Figure 6(d) shows that the corresponding vertical component exhibits a similar organization to its first mode counterpart. Therefore, the simple model described by the second eigenmode is that streamwise-elongated regions of alternating sign within the incoming boundary layer correspond to an undulating behaviour of the reflected shock foot.

Higher-order eigenmodes exhibit more complicated features. Figure 6(e) depicts the streamwise component of mode 3. It shows a bifurcation into three large-scale regions of relatively uniform opposed streamwise velocity fluctuations that are oriented parallel to the wall and elongated in the streamwise direction. The width of these regions is approximately 0.6δ, and they extend the streamwise length of the measurement domain. This eigenmode therefore represents the higher-order harmonics of the spanwise rippling component of the reflected shock foot patterns.

Figure 6(g) depicts the streamwise component of mode 4. It shows a bifurcation into four regions of streamwise velocity fluctuations of alternating sign within the redeveloping boundary layer, demonstrating that bifurcations can take place locally within an eigenmode. Such behaviour has also been observed in a 2D POD of the interaction carried out by Humble *et al.* [19] using PIV data in the streamwise–wall-normal plane, and is thought to be associated with a shedding process that is observed to take place downstream of the separation bubble. This behaviour is not intuitively obvious from the instantaneous realizations. It is now clear that the eigenmodes can be viewed as a family of modes, each containing subspace representations of the phenomenology observed in the instantaneous realizations that pertain to the most dominant components of a complex dynamical process.
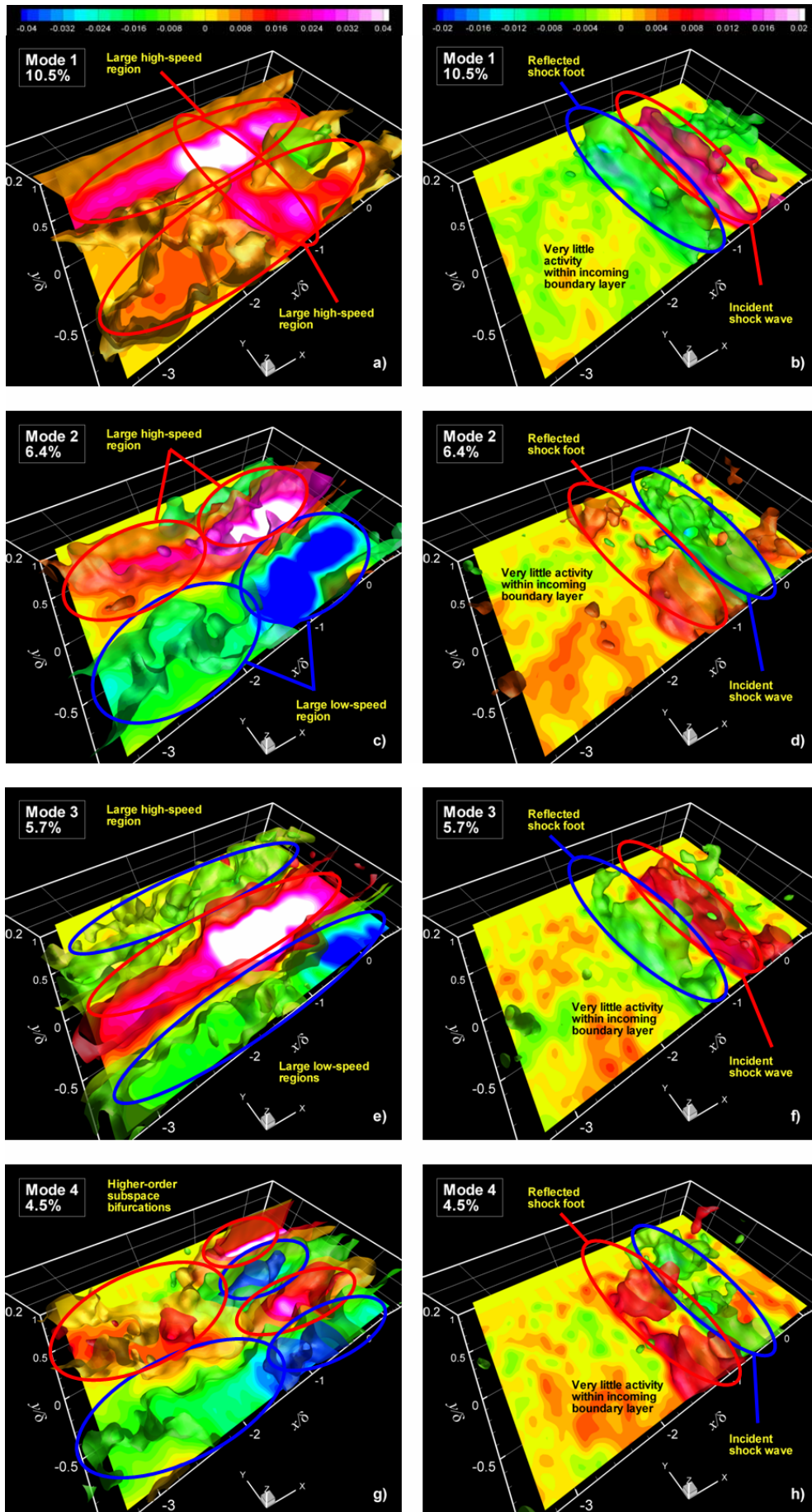
Figure 6. Global POD eigenmodes: (left) u'/U_∞; (right) w'/U_∞. Modal energy is shown inset. (Note: modes ≥ 2 shows $2u'/U_\infty$)

735

Conclusions

An experimental study has investigated the 3D instantaneous flow organization of an incident SWTBLI using tomographic PIV in combination with data processing using the POD. The results show that the incoming boundary layer contains large-scale coherent motions, in the form of streamwise-elongated regions of low- and high-speed fluid, similar to what has been observed in incompressible turbulent boundary layers. The instantaneous reflected shock foot pattern appears to respond to these regions as they enter the interaction, conforming to the low- and high-speed regions. Its behaviour can be qualitatively decomposed into two types of patterns: an overall streamwise translation and a spanwise rippling. These observations are substantiated by the global POD eigenmodes, which contain subspace representations of this phenomenology.

Acknowledgments

References

[1] Adamson, T. C. Jr. & Messiter, A. F. 1980 Analysis of two-dimensional interactions between shock waves and boundary layers, *Annu. Rev. Fluid Mech.* **12**, pp. 103−138.

[2] Aubry, N., Holmes, P., Lumley, J.P. & Stone, E. 1988 The dynamics of coherent structures in the wall region of the turbulent boundary layer, *J. Fluid Mech.* **192**, pp. 115−173.

[3] Beresh, S. J., Clemens, N. T. & Dolling, D. S. 2002 Relationship between upstream turbulent boundary-layer velocity fluctuations and separation shock unsteadiness, *AIAA J.* **40**, pp. 2412−2422.

[4] Berkooz, G., Holmes, P. & Lumley, J. L. The proper orthogonal decomposition in the analysis of turbulent flows, *Annu. Rev. Fluid Mech.* **25**, pp. 539−575.

[5] Délery, J. & Marvin J. G. 1986 Shock-wave boundary layer interactions, AGARDograph 280.

[6] Dolling, D. S. 2001 Fifty years of shock wave/boundary layer interaction research: what next? *AIAA J.* **39**, pp. 1517−1531.

[7] Elsinga, G. E., Adrian, R. J., van Oudheusden, B. W. & Scarano, F. 2007 Tomographic-PIV investigation of a high reynolds number turbulent boundary layer, In proc. *7th Int. Symp. on Particle Image Velocimetry*, Rome, Italy, Sep. 11–14.

[8] Elsinga, G. E., Kuik, D. J., van Oudheusden, B. W. & Scarano, F. 2007 Investigation of the three-dimensional coherent structures in a turbulent boundary layer with tomographic-PIV, In proc. *45th AIAA Aerospace Sciences Meeting & Exhibit*, Reno, NV, Jan 8−11.

[9] Elsinga, G. E., Scarano, F., Wieneke, B. & van Oudheusden, B. W. 2006 Tomographic particle image velocimetry, *Exp. Fluids* **41**, pp. 933–947.

[10] Erengil, M. E. & Dolling, D. S. 1993 Physical causes of separation shock unsteadiness in shock wave/turbulent boundary layer interactions, AIAA paper 93-3134.

[11] Ganapathisubramani, B., Clemens, N. T. & Dolling, D. S. 2007 Effects of upstream boundary layer on the unsteadiness of shock-induced separation, *J. Fluid Mech.* **585**, pp. 369−394.

[12] Ganapathisubramani, B., Clemens, N. T. & Dolling, D. S. 2006 Large-scale motions in a supersonic turbulent boundary layer, *J. Fluid Mech.* **556**, pp. 271−282.

[13] Ganapathisubramani, B., Longmire, E. K. & Marusic, I. 2003 Characteristics of vortex packets in turbulent boundary layers, *J. Fluid Mech.* **478**, pp. 35−46.

[14] Green, J. E. 1970 Interactions between shock waves and turbulent boundary layers, *Prog. Aero. Sci.* **11**, pp. 253−340.

[15] Hankey, W. L. Jr. & Holden, M. S. 1975 Two-dimensional shock-wave boundary layer interactions in high-speed flows, AGARDograph 203.

[16] Herman, G. T. & Lent, A. 1976 Iterative reconstruction algorithms, *Comput. Biol. Med.* **6**, pp. 273−294.

[17] Holmes, P., Lumley, J. L. & Berkooz, G. 1996 Turbulence, coherent structures, dynamical systems and symmetry, Cambridge Univ. Press, United Kingdom.

[18] Humble, R. A., Scarano, F. & van Oudheusden, B. W. 2007 Particle image velocimetry measurements of a shock wave/turbulent boundary layer interaction, *Exp. Fluids* **43**, pp. 173–183

[19] Humble, R. A., Scarano, F. & van Oudheusden, B. W. 2007 Unsteady flow organization of a shock wave/turbulent boundary layer interaction, In proc. *IUTAM Symp. on Unsteady Separated Flows and their Control*, Corfu, Greece, Jun. 18−22.

[20] Jeong, J., Hussain, F., Schoppa, W. & Kim, J. 1997 Coherent structures near the wall in a turbulent channel flow, *J. Fluid Mech.* **332**, pp. 353−396.

[21] Moreno, D., Krothapalli, A., Alkislar, M. B. & Lourenco, L. M. 2004 Low-dimensional model of a supersonic rectangular jet, *Phys. Rev. E* **69**, 026304.

[22] van Oudheusden, B. W., Scarano, F., van Hinsberg, N. P. & Watt, D. W. 2005 Phase-resolved characterization of vortex shedding in the near wake of a square-section cylinder at incidence, *Exp. Fluids* **39**, pp. 86−98.

[23] Pirozzoli, S. & Grasso, F. 2006 Direct numerical simulation of impinging shock wave/turbulent boundary layer interaction at *M*=2.25, *Phys. Fluids* **18**, 065113.

[24] Scarano, F. 2002 Iterative image deformation methods in PIV, *Meas. Sci. and Technol.,* **13**, R1−R19.

[25] Schröder, A., Geisler, R., Elsinga, G. E., Scarano, F. & Dierksheide, U. 2007 Investigation of a turbulent spot and a tripped turbulent boundary layer using time-resolved tomographic PIV, *Exp. Fluids* (in press).

[26] Sirovich, L. 1987 Turbulence and the dynamics of coherent structures, Q. Appl. Math. **XLV**, pp. 561−571.

[27] Smits, A. J. & Dussauge, J. P. 2006 Turbulent shear layers in supersonic flow. 2nd Ed. American Institute of Physics, New York.

[28] Tomkins, C. D. & Adrian, R. J. 2003 Spanwise structure and scale growth in turbulent boundary layers, *J. Fluid Mech.* **490**, pp. 37−74.

[29] Ünalmis, Ö.H. & Dolling, D.S. 1998 Experimental study of causes of unsteadiness in shock wave/turbulent separation, *AIAA J.* **36**, pp. 371−378.

[30] Wieneke, B. 2007 Volume self-calibration for stereo-PIV and tomographic-PIV, In proc. *7th Int. Symp. on Particle Image Velocimetry*, Rome, Italy, Sep. 11−14.

[31] Wu, M. & Martin, M. P. 2007 Analysis of shock motion in shockwave/turbulent boundary layer interaction using direct numerical simulation data, *J. Fluid Mech.* (in press).

[32] Zhou, J., Adrian, R. J., Balachandar, S. & Kendall, T. M. 1999 Mechanisms for generating coherent packets of hairpin vortices in channel flow, *J. Fluid Mech.* **387**, pp. 353−396.